Research on Engineering Structures & Materials
www.jresm.org
MIM Research Group

Research Article

Seismic frequency content as a key parameter in the dynamic buckling behavior of tall thin-walled steel tanks

Mounia Menoun Hadj Brahim [*,1,a], Imed Bennoui [1,b], Mohammed Djermane [2,c]

[1]*National Center of Studies and Integrated Research on Building Engineering (CNERIB), Algiers, Algeria*
[2]*FIMAS Laboratory, University of Tahri Mohamed Bechar, 08000, Algeria*

Article Info

Article History:

Received: 19 Oct 2025

Accepted: 11 May 2026

Keywords:

Dynamic buckling;
Thin-walled steel tanks;
Frequency content;
Peak ground acceleration;
Seismic design standards

Abstract

The dynamic buckling behavior of anchored thin-walled steel storage tanks subjected to seismic excitation is investigated, with particular emphasis on the influence of seismic frequency content. Nonlinear analyses are performed on a representative anchored cylindrical tank with an aspect ratio H/D=2, selected for its practical relevance and known susceptibility to diamond-shaped local buckling. Three recorded ground motions with distinct frequency characteristics -Boumerdes, -Parkfield, and -San Fernando, are employed to evaluate their effects on seismic response and buckling of tank. The numerical results reveal the development of diamond-shaped local buckling modes concentrated in the upper shell courses, with buckling occurring at PGA levels of 0.16 g, 0.11 g, and 0.76 g for the Boumerdes, Parkfield, and San Fernando records, respectively. These findings demonstrate that earthquake frequency content plays a governing role in the dynamic stability of thin-walled steel storage tanks and should be explicitly considered in seismic response and buckling assessments.

1. Introduction

Earthquakes are among the most destructive natural hazards, although only a limited number of seismic events lead to severe structural damage. Experience from past earthquakes has shown that liquid-containing steel storage tanks are particularly vulnerable to seismic excitation, often suffering extensive damage that renders them inoperative. Post-earthquake investigations following major seismic events in Turkey and India documented critical failure modes in petroleum steel storage tanks, including shell buckling, roof and anchorage damage, foundation distress, and hydrodynamic pressure–induced effects. These studies further indicate that steel tanks exhibit greater vulnerability than reinforced concrete tanks when subjected to comparable seismic demands[1,2]. Among the observed damage mechanisms, dynamic buckling of the tank wall has consistently been identified as the most frequent and severe failure mode, governing the seismic safety of slender tank configurations. his behavior has been repeatedly observed during major earthquakes, including the Long Beach (1933), Kern County (1952), and Kobe (1995) events, which further revealed the inherent susceptibility of steel tanks to dynamic instability when subjected to seismic loading [3].

These observations emphasized the dominant role of fluid–structure interaction effects, in which the coupled response of structural vibrations and hydrodynamic pressures is highly sensitive to the frequency content of the seismic excitation. Consequently, significant research efforts have been devoted to understanding the dynamic response, instability mechanisms, and seismic fragility of thin-walled steel tanks under earthquake excitation.

*Corresponding author: m.hadjbrahim@cnerib.edu.dz
[a]orcid.org/0000-0002-2236-6607; [b]orcid.org/0009-0009-4777-7742; [c] orcid.org/0000-0003-1267-1787
DOI: http://dx.doi.org/10.17515/resm2026-1277st1019rs

Accordingly, the dynamic behavior of cylindrical shells containing fluid has been the subject of numerous analytical, numerical, and experimental investigations. Zhang et al. [4]developed a finite element formulation based on the classical shell theory and potential flow theory, which was validated with published experimental results. The influence of flow velocities, hydrostatic pressures and boundary conditions on natural frequencies has also been addressed. Shen et al. [5]for instance, investigated cylindrical shells under combined axial compression and external pressure, demonstrating the sensitivity of buckling response to initial imperfections. In addition, comprehensive reviews by Virella et al. [6–8]synthesized research on buckling behavior, foundation settlement, and fire resistance of steel tanks, with particular emphasis on dynamic loading conditions such as wind and earthquakes.

Several numerical investigations have focused on the seismic instability of steel storage tanks and their assessment within the framework of existing design codes. Buratti and Tavano [9]examined the seismic fragility of fixed-base tanks using an added-mass approach to represent fluid–structure interaction, confirming its effectiveness in predicting buckling behavior. Djermane et al. [10]evaluated seismic design provisions prescribed by AWWA D100 and Eurocode 8, reporting satisfactory performance for broad tanks while highlighting notable limitations when applied to slender configurations. Furthermore, the seismic response of anchored tanks subjected to combined horizontal and vertical ground-motion components was investigated by Sobhan [11,12], who demonstrated that explicit consideration of vertical acceleration leads to more accurate predictions of buckling capacity and deformation demand.

Beyond code-based evaluations, recent investigations have increasingly emphasized the fundamental mechanisms governing dynamic buckling of thin-walled structures under extreme excitation. Çelik and Köse [13], numerically examined the seismic buckling response of thin-walled steel tanks, highlighting the influence of roof geometry and shell thickness on deformation patterns and instability onset. Wind-induced dynamic buckling was investigated experimentally and numerically by Yasunaga and Uematsu [14], showing that shell vibration plays a crucial role in instability, while inertial effects remain secondary under certain loading conditions. The influence of vertical seismic excitation on raised conical tanks was explored by Hadj Djelloul et al.[15], underscoring the importance of vertical acceleration components in seismic stability assessments.

In parallel, the effects of anchorage conditions and geometric slenderness on seismic stability have been widely investigated. Through three-dimensional nonlinear finite element analyses, it was demonstrated by Moreno et al. [16], that anchorage configuration strongly affects stress distribution and buckling capacity, particularly for slender tanks, for which existing design codes may be unconservative. Although a marked decrease in buckling strength with increasing radius-to-thickness ratio was reported by Ullah and Mamaghani [17]confirming the governing role of geometric slenderness in seismic stability.

Complementing these investigations, the seismic response of cylindrical storage tanks subjected to ground motions with varying frequency content was examined by Abd-Elhamed et al. [18], with explicit consideration of fluid–structure–soil/foundation interaction. It was demonstrated that Low-frequency ground motions generally induce a smaller response than high-frequency motions, although soil–tank interaction can still amplify the resulting response. More recently, a comparative review of recent research, design recommendations, standards, and seismic codes for large liquid storage tanks was provided by Nadjuri et al. [19], in which the limitations of existing guidelines in capturing complex tank–fluid–soil interactions and dynamic buckling behavior were highlighted.

Collectively, these studies indicate that current design codes and simplified seismic evaluations may not fully account for the frequency-sensitive dynamic behavior of anchored thin-walled steel tanks, highlighting the need for detailed numerical investigations of critical seismic loading and associated buckling mechanisms. The seismic performance of these tanks is strongly influenced by both structural geometry and ground motion characteristics: tall cylindrical tanks are particularly susceptible to local diamond-shaped buckling, whereas broader tanks tend to develop elephant-foot deformations, as confirmed by experimental studies and post-earthquake observations, such as the 1980 Livermore event. To address these challenges, the present study employs nonlinear

numerical simulations to investigate the dynamic buckling behavior of a representative anchored tank with an aspect ratio (H/D) of 2. The investigation aims to determine the critical horizontal acceleration associated with the initiation of buckling and to assess the influence of seismic frequency characteristics on structural response. The selected tank geometry reflects a commonly adopted and economically efficient design, while its susceptibility to diamond-shaped local buckling provides a relevant benchmark for future studies on mitigation strategies, including the potential implementation of stiffening rings.

2. Seismic Modeling of Steel Storage Tanks

2.1 Tank Design, Geometry, and Hydrodynamic Assumptions

To investigate the influence of seismic motion frequency characteristics on the dynamic response of tall steel storage tanks, a representative slender cylindrical tank with a height-to-diameter ratio (H/D) of 2 was selected for analysis (Fig. 1 (a)). The adopted tank configuration is explicitly defined, and its selection is justified by both economic factors and site space requirements, while its susceptibility to diamond-shaped local buckling under seismic excitation is clearly identified [7,10].

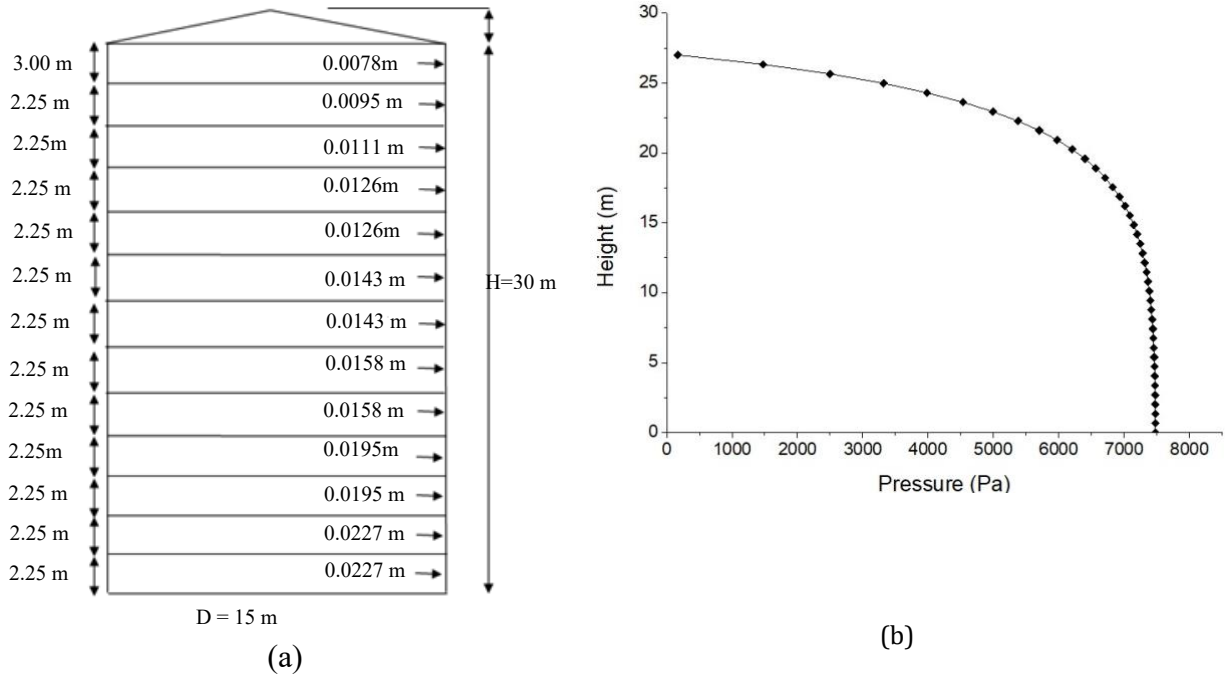

Fig. 1. Schematic of a tall cylindrical tank (H/D = 2) showing the (a) geometry and (b) variation of impulsive hydrodynamic pressure

The modeling assumptions were carefully defined to capture the coupled fluid–tank interactions and to provide an accurate representation of the tank's dynamic response under seismic excitation. Following Housner's formulation, adopted in Eurocode 8 (EN 1998-4) [20] and API 650 [21], the hydrodynamic response of liquid-filled tanks is represented by impulsive and convective components. Due to the large separation of their natural periods, these components were treated as uncoupled, with the response dominated by the impulsive component. Three-dimensional finite element model was developed considering only the impulsive interaction, while convective effects were neglected, consistent with previous studies[6]. All translational and rotational degrees of freedom at the tank base were restrained, except for horizontal displacement in the direction of seismic excitation, and horizontal ground motion was applied along the x-axis to simulate the earthquake.

The tank shell thickness was determined following API 650 provisions, assuming a fill level of 90% of the total tank height. The contained fluid was modeled using an equivalent density approach, in which the hydrodynamic added mass of the liquid was incorporated into an effective density assigned to the tank shell. Equivalent density values were evaluated based on the impulsive

hydrodynamic pressure, following the formulations proposed by Veletsos and Shivakumar and subsequently adopted by Virella et al. [7], as illustrated in Fig. 1 (b).

$$P_i = (\eta, \theta, t) = c_i(\eta)\rho R\, \ddot{x}_g\,(t)\cos\theta \tag{1}$$

According to Virella et al., the function ci (η) which describes the distribution of impulsive pressure over the cylinder height and is calculated as follows:

$$c_i(\eta) = 1 - \sum_{n=1}^{\infty} c_{cn}(\eta) \tag{2}$$

$$c_{nc}(\eta) = \frac{2}{\lambda_n^2 - 1}\left(\frac{\cosh[\lambda_n(H/R)\eta]}{\cosh[\lambda_n(H/R)]}\right) \tag{3}$$

Where; the symbol λn corresponds to the nth solution of the equation obtained from the derivative of the Bessel function. The first three roots of this equation are: λ1 = 1.841, λ2 = 5.311, and λ3 = 8.536. η = z /H; z is defined as the height taken from the tank base upward.

A simplified technique to account for fluid–structure interaction was proposed by Barton et al. (1987), in which an equivalent density was assigned to the tank shell section submerged beneath the liquid level. This equivalent density was defined to represent both the mass of the steel shell up to that level and the impulsive fluid mass as described by Housner [6,10,15] . The method was subsequently adopted and refined by Nachtigall et al. [8], enabling the equivalent density to be evaluated for the tank wall [10]as follows:

$$\rho *_s = \frac{Mass\ of\ the\ liquid + \ \ Mass\ of\ the\ wall\ shell\ of\ the\ tank}{the\ volume\ of\ the\ wall\ of\ the\ tank} \tag{4}$$

2.2 Analytical Approach

Assuming a 3D FE approach for structural simulation, the dynamic performance characteristics of the system can be described by the equation governing the system's equilibrium:

$$[M]\left\{\frac{d^2u}{d^2t}\right\} + [C]\left\{\frac{du}{dt}\right\} + [K]\{u(t)\} = -F(t) \tag{5}$$

Where; the matrices [M], [C] and [K] refer to the mass, damping and stiffness properties of the structure analyses, when the matrixes K and C are to be identified. According to Eurocode 3 part 1-6 correspond to Strength and Stability of Shell Structures[22], the structural analyses should be performed with consideration of both geometric and material nonlinear effects. To determine the elasto-plastic behavior of an isotropic steel material, the formula given below is used [23].

$$\sigma_u = \sigma_y + \varepsilon_{pl1} * k \tag{6}$$

Where; k is adopted as 0.0036*E and elastic modulus E equal to 210 GPa. Linear-elastic up to a first yield stress of σy = 250 MPa, followed by 0.36% linear strain hardening up to an ultimate stress of σu = 400 MPa. Rayleigh damping was used to attempt the nonlinear analysis, where the damping matrix [C] is formulated as follows:

$$[C] = (\alpha_M)[M] + (\beta_K)[K] \tag{7}$$

Where; αM and βk denote the mass-proportional and stiffness-proportional damping coefficients respectively. The value of αM and βk which corresponds to the constant value of ξi, can be calculated from two modes and so on for the other modes. This procedure conserved the value of damping for modes with natural periods rang between the border corresponding to the highest participation factors along the translational axes. Generally, for steel tanks, ξi, is expected to be of the order of 2% for impulsive mode [23]. The additional effect of radiation damping is neglected in this study where the foundation is not included in the simulation:

$$\xi_i = \frac{1}{2\omega_i}\alpha_M + \frac{\omega_i}{2}\beta_K \tag{8}$$

The external force applied to the storage tanks containing fluids corresponds to the combined contribution of the structural and liquid masses, each subjected to seismic loading.

$$F(t) = [M_s]\{r_x\}\ddot{x}g(t) + \{P_i\}\ddot{x}g(t) \tag{9}$$

$$\ddot{x}g(t) = PGA * f(t) \tag{10}$$

In the equation (5), {u(t)}, {ú(t)} and {ü (t)} denote to the displacement, velocity and acceleration vectors respectively, some hypotheses are made to solve the equation (1), like respect to the nature and direction of the incident motion. Where [rx] is an n-dimensional influence vector, with entries of '1' assigned to the degrees of freedom corresponding to the direction of ground excitation, and '0' elsewhere, {Pi} denotes the vector of nodal forces induced by an acceleration of 1g, representing the impulsive component of the hydrodynamic pressure acting on the system. Here, [M_s] stands for the shell mass matrix, and f(t) indicates the earthquake time history.

2.3 Modeling and Finite Element Mesh

The continuous advancement of computational power and numerical techniques has enabled robust software tools to solve highly nonlinear equilibrium and instability problems in structural systems. In this study, nonlinear dynamic analyses were performed using the explicit time integration scheme available in ABAQUS/Explicit [24]. Unlike implicit algorithms, which require iterative procedures and may encounter difficulties with strong nonlinearities, the explicit approach is conditionally stable and free from convergence issues, making it particularly suitable for problems involving severe material and geometric nonlinearities, despite potentially longer computation times. The solver was employed to investigate the seismic buckling behavior of slender steel storage tanks.

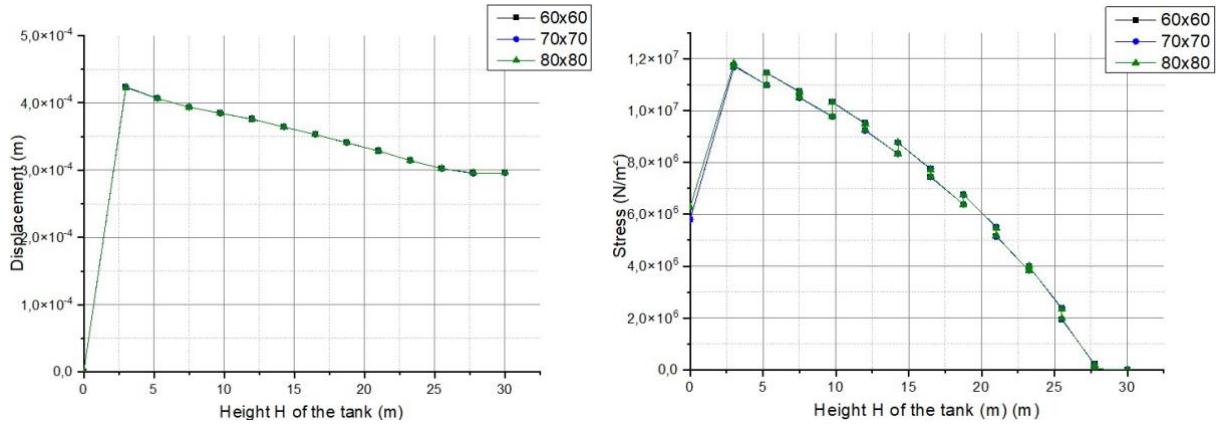

(a) (b)

Fig. 2. Mesh sensitivity analysis under static loading: (a) displacement distribution along the tank height; (b) axial stress distribution for different mesh densities.

The adequacy of the finite element discretization was verified through a mesh sensitivity analysis conducted under both static (hydrostatic) and dynamic (seismic) loading conditions, with an empty tank considered for the dynamic analysis. In the static analyses, a mesh sensitivity study was performed by varying the characteristic element size along the tank height, adopting 60×60, 70×70, and 80×80 discretization. The resulting displacement and stress distributions were compared in order to assess convergence. As shown in Fig. 2(a) and (b), only minor differences were observed between the responses obtained with the refined meshes, indicating adequate convergence of the numerical solution.

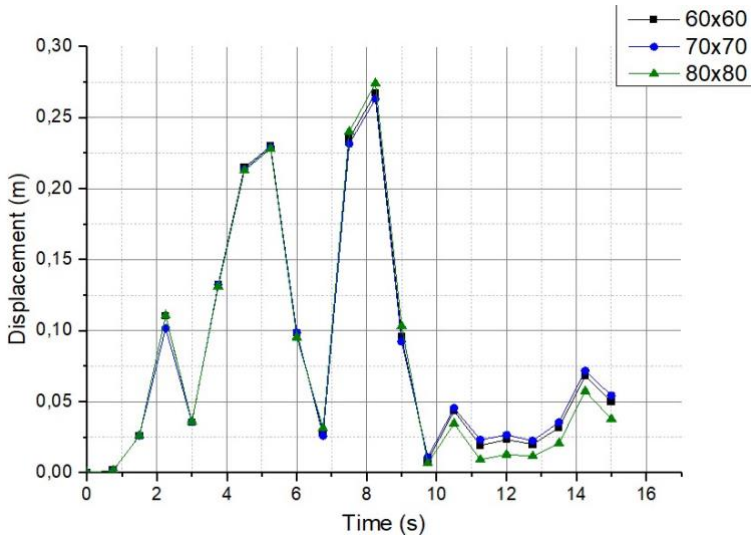

Fig. 3. Mesh sensitivity analysis under dynamic loading: comparison of shell displacement time histories obtained using 60×60, 70×70, and 80×80 meshes

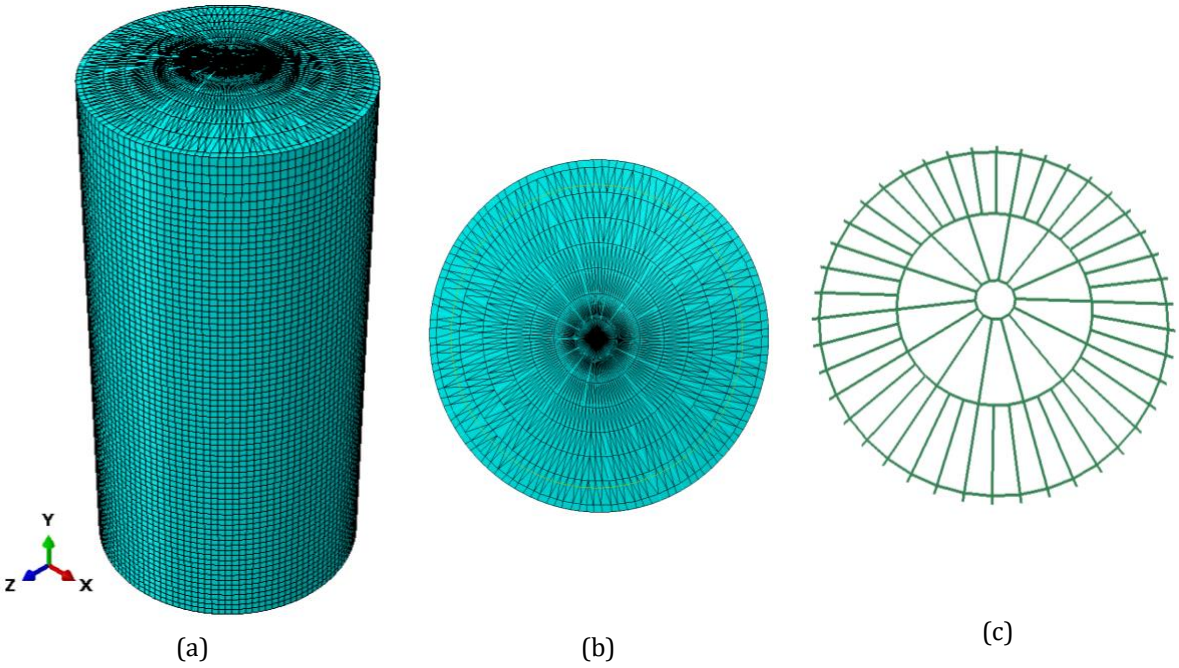

(a) (b) (c)

Fig. 4. Finite element mesh geometry of the tank showing: (a) Cylindrical steel shell discretized with four-node reduced-integration shell elements (S4R), (b) Roof modeled with triangular shell elements (S3), and (c) Rafters represented using beam elements (B31)

For the dynamic analyses, the displacement vs time histories corresponding to the different mesh densities exhibited nearly identical response trends and peak amplitudes (Fig. 3). Based on these findings, the 70×70 mesh was selected for subsequent simulations, as it ensures sufficient accuracy while maintaining reasonable computational efficiency. Based on the selected mesh, the finite element discretization was composed of 12,026 elements, including 10,080 four-node reduced-integration shell elements (S4R) for the cylindrical shell, which are particularly suitable for thin-walled structures; 1,638 three-node triangular shell elements (S3) for the roof; and 308 two-node beam elements (B31) for the roof rafters (Fig. 4). Both geometric and material nonlinearities were considered. Large-deformation effects were accounted for by activating the NLGEOM option in ABAQUS, allowing the stiffness matrix to be continuously updated as the geometry evolved.

2.4 Seismic Input Motions, Frequency Characteristics and Scaling Procedure

Seismic records were selected based on key characteristics, including peak ground acceleration (PGA), duration, and frequency content. To reduce computational cost in nonlinear dynamic analyses, short-duration records capturing essential amplitudes and frequencies were preferred. It has been demonstrated in previous studies that the buckling behavior of tanks can be adequately evaluated using three carefully selected ground motions while maintaining computational efficiency [10,18,25,26]. Accordingly, three representative earthquakes were adopted to cover intermediate- and high-frequency excitations: San Fernando (1971), Boumerdes (Dar El Beida, 2003), and Parkfield (1966) (Fig. 5).

To quantitatively characterize the frequency content of the selected records, the PGA/PGV ratio-defined as the ratio between peak ground acceleration and peak ground velocity-was employed as a basic indicator of earthquake frequency characteristics. Records with PGA/PGV ratios greater than 1.2 are classified as high-frequency motions, whereas those with ratios lower than 0.8 are categorized as low-frequency motions. Motions with PGA/PGV ratios between 0.8 and 1.2 are considered to exhibit intermediate-frequency content. Based on this classification, the selected ground motions span distinct frequency ranges, as summarized in Table 1, enabling a systematic investigation of the influence of ground-motion frequency content on the dynamic buckling behavior of thin-walled steel storage tanks, beyond the effects of peak ground acceleration (PGA) alone.

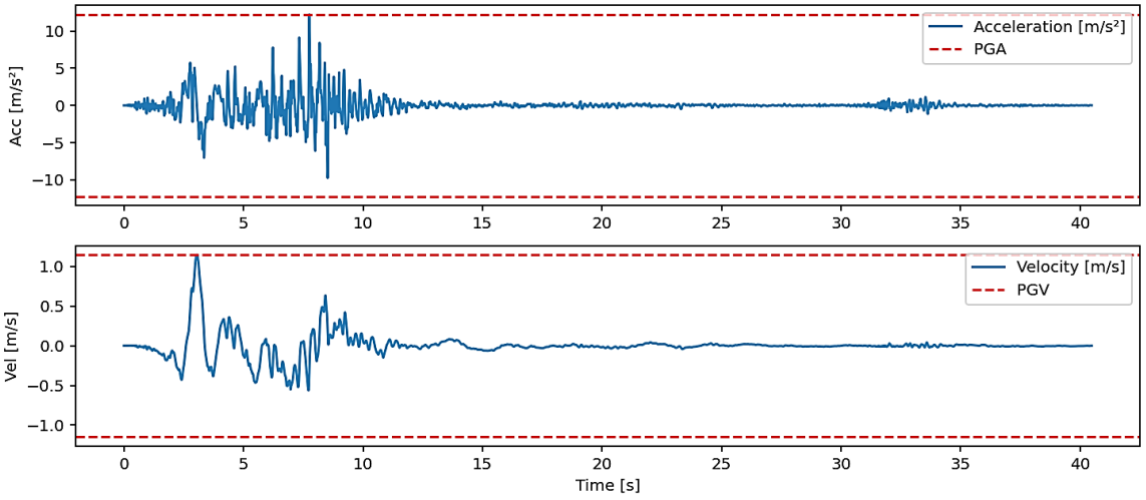

(a)

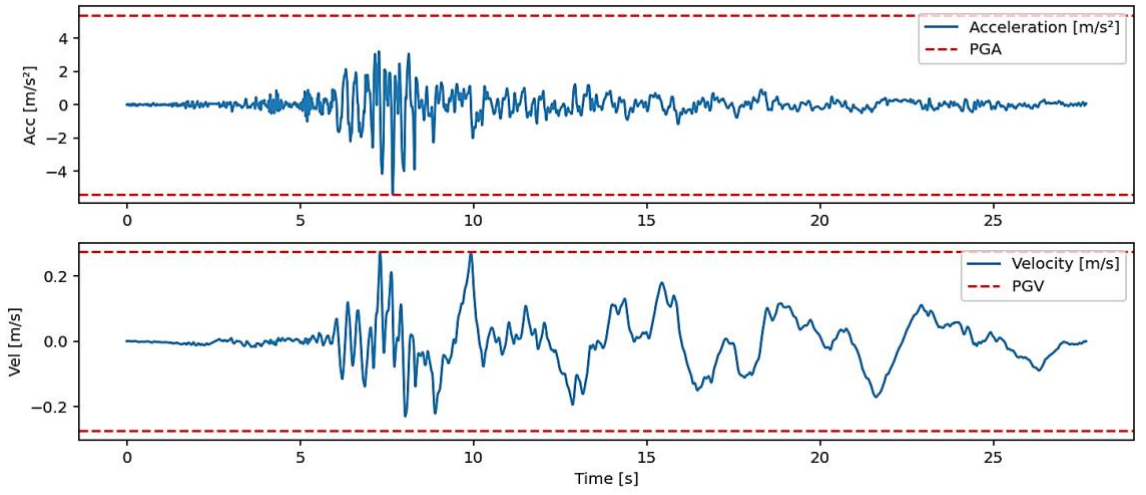

(b)

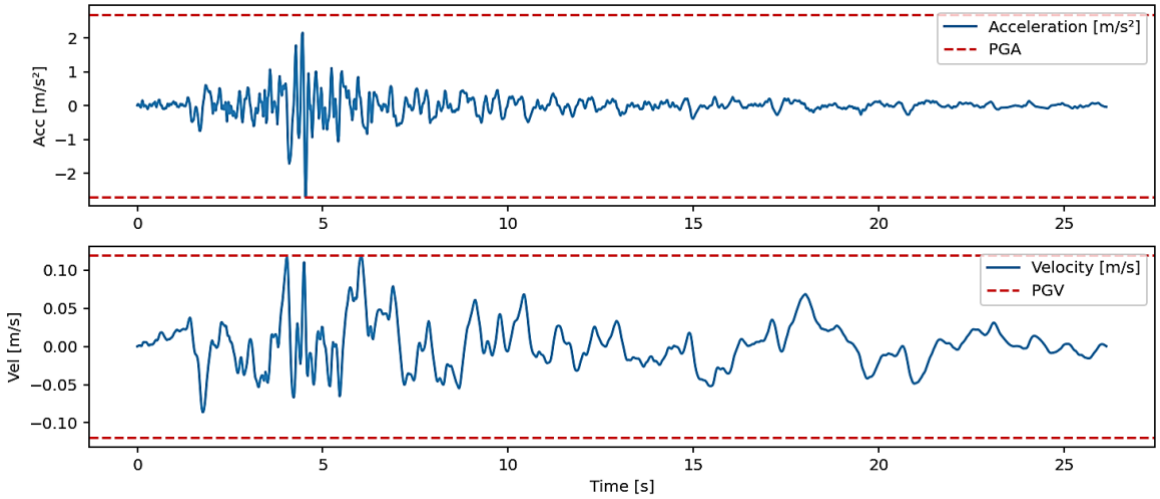

(c)

Fig. 5. Acceleration and velocity time histories of the selected earthquake ground motions considered in this study: (a) San Fernando earthquake (1971), (b) Boumerdes earthquake (2003, Dar El Beida station), and (c) Parkfield earthquake (1966).

Table 1. Seismic intensity measures

Earthquake Record	Δt (s)	Duration (s)	PGA (m/s^2, g)	PGV (m/s)	PGA/PGV (g·s/m)	Dominant Frequencies
San Fernando (1971, S–W)	0.010	40.48	12.26 (1.25 g)	1.15	1.09	Intermediate
Boumerdes (2003, E–W)	0.005	27.68	5.40 (0.55 g)	0.275	2.00	High + some long
Parkfield (1966, NOAA Usaca)	0.020	26.14	2.70 (0.27 g)	0.120	2.30	High / short-period

A comparative overview of three seismic records-the San Fernando (1971, S–W), Boumerdes (2003, E–W), and Parkfield (1966)-highlights differences in frequency content and PGA/PGV ratios. The San Fernando record is dominated by intermediate frequencies with a low PGA/PGV ratio of 1.09. Boumerdes exhibits a mixed spectrum containing both high- and long-period energy, with a moderate PGA/PGV ratio of 2.00. The Parkfield record is rich in high-frequency, short-period content and has the highest PGA/PGV ratio of 2.30. These distinctions emphasize how the frequency content and PGA/PGV ratio vary among seismic events, providing a clear comparative characterization of these ground motions.

The corresponding Fourier amplitude spectra of these ground motions are shown in Fig. 6. Consistent with the previous characterization, the San Fernando (1971) record exhibits dominant energy at low to intermediate frequencies, with most spectral amplitudes concentrated below approximately 5 Hz and a principal peak around 2–3 Hz. The Boumerdes (2003) record is dominated by high-frequency content and long-period components, mainly between 2 and 4 Hz, with a dominant peak near 3 Hz, reflecting pronounced regional near-field effects. In contrast, the Parkfield (1966) ground motion is rich in high-frequency, short-period content, with most energy concentrated above 5 Hz and several smaller peaks spread across 5–10 Hz, generally showing sharper, impulsive characteristics compared to the San Fernando and Boumerdes records. These spectral distinctions complement the PGA/PGV-based comparison, highlighting the variability in frequency content among the three seismic events.

The recorded earthquake ground motions were scaled using a PGA-based normalization and scaling procedure. Each accelerogram was first normalized by its original peak ground acceleration (PGA) by applying a constant scale factor equal to the inverse of the original PGA, resulting in a normalized record with unit PGA.

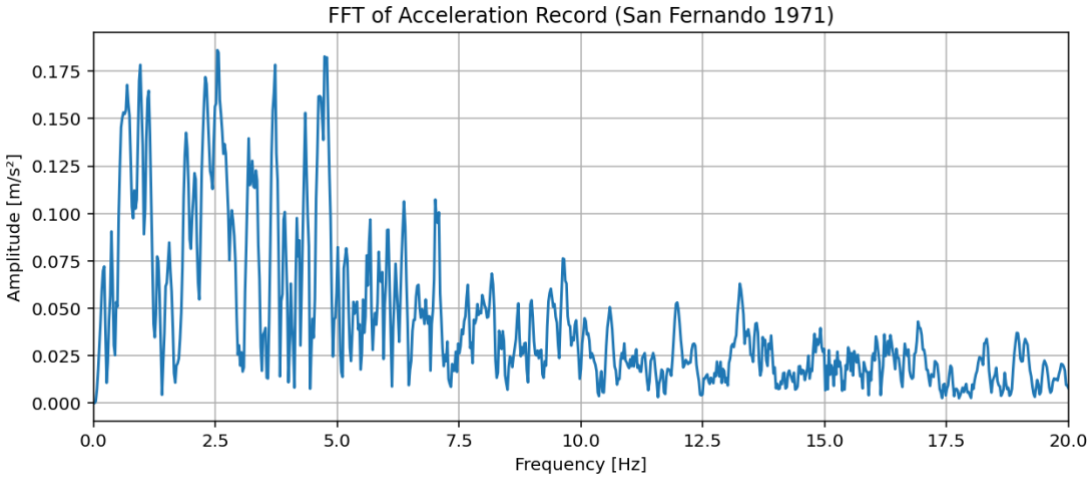

(a)

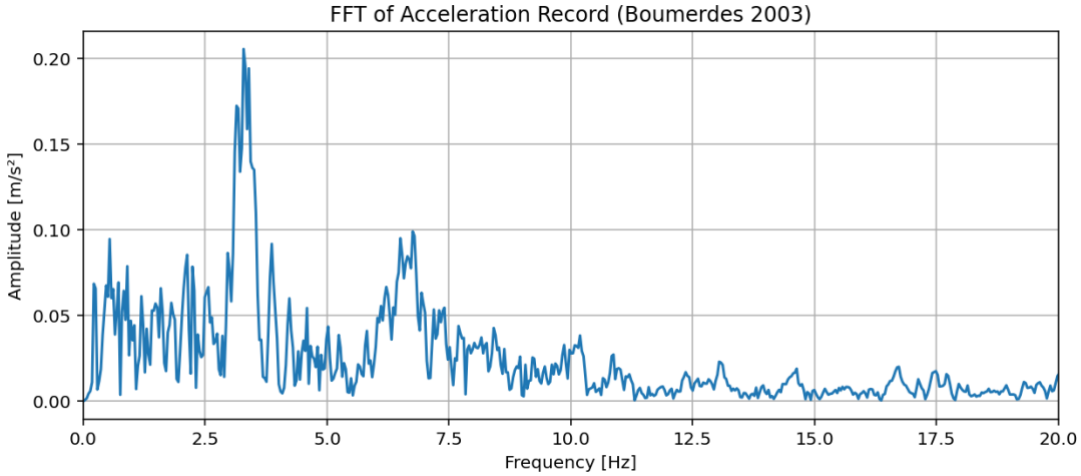

(b)

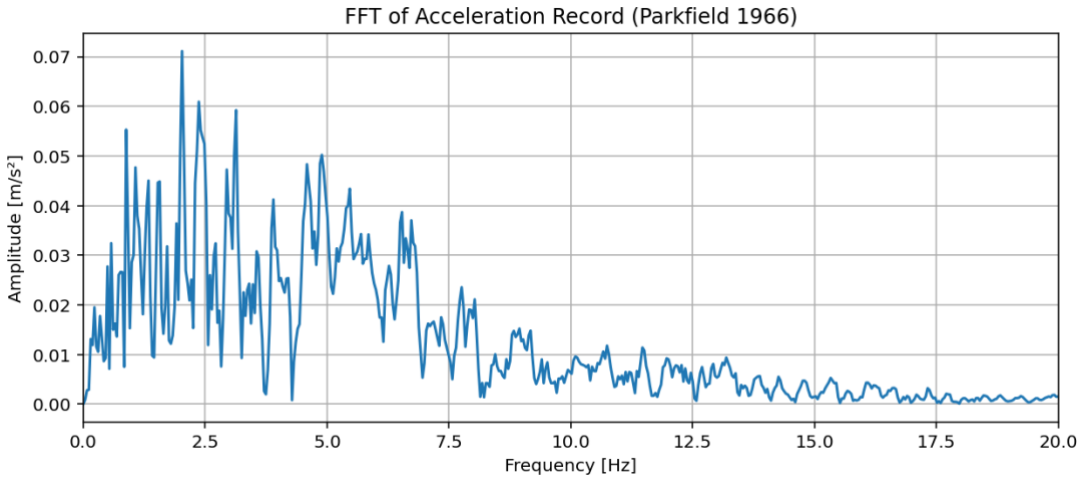

(c)

Fig. 6. Fourier amplitude spectra of the accelerograms: (a) San Fernando 1971, (b) Boumerdes 2003 (Dar El Beida), and (c) Parkfield 1966.

The normalized accelerograms were then multiplied by a target PGA value to achieve the desired intensity level. Incremental scaling was subsequently applied by progressively increasing the target PGA until the onset of buckling was observed. The PGA corresponding to the first occurrence of buckling was identified as the critical PGA associated with each earthquake record. This two-

step scaling procedure preserves the original temporal characteristics, frequency content, and duration of the ground motions, ensuring that only the amplitude of the excitation is modified.

3. Results of Analysis and Discussion

3.1 Buckling Onset and Critical PGA

Seismic-induced buckling of steel tanks is generally classified as either elastic or elasto-plastic dynamic buckling, as confirmed by experimental and numerical studies [10,15]. The critical dynamic load can be evaluated using three commonly applied criteria. The first, proposed by Budiansky and Roth [27], is based on Liapunov stability: time–displacement curves are plotted for increasing PGA values, and the critical PGA is identified as the curve exhibiting a sudden "jump" relative to neighboring curves, indicating the onset of dynamic buckling. The second criterion employs phase-plane trajectories (U, Ú), where stable trajectories remain confined near the static equilibrium point, which acts as a center of attraction; at the critical load, trajectories diverge from this equilibrium point without oscillating around it, indicating the onset of instability. The third, the Pseudo-Equilibrium Path method, originally proposed by Budiansky and Roth and later generalized by Ari-Gur and Simonetta, relates the peak deflection to the pulse intensity. In the present study, elastic buckling was observed at the upper portion of the cylindrical shell, and the critical peak ground acceleration (PGAc) was determined using all three criteria.

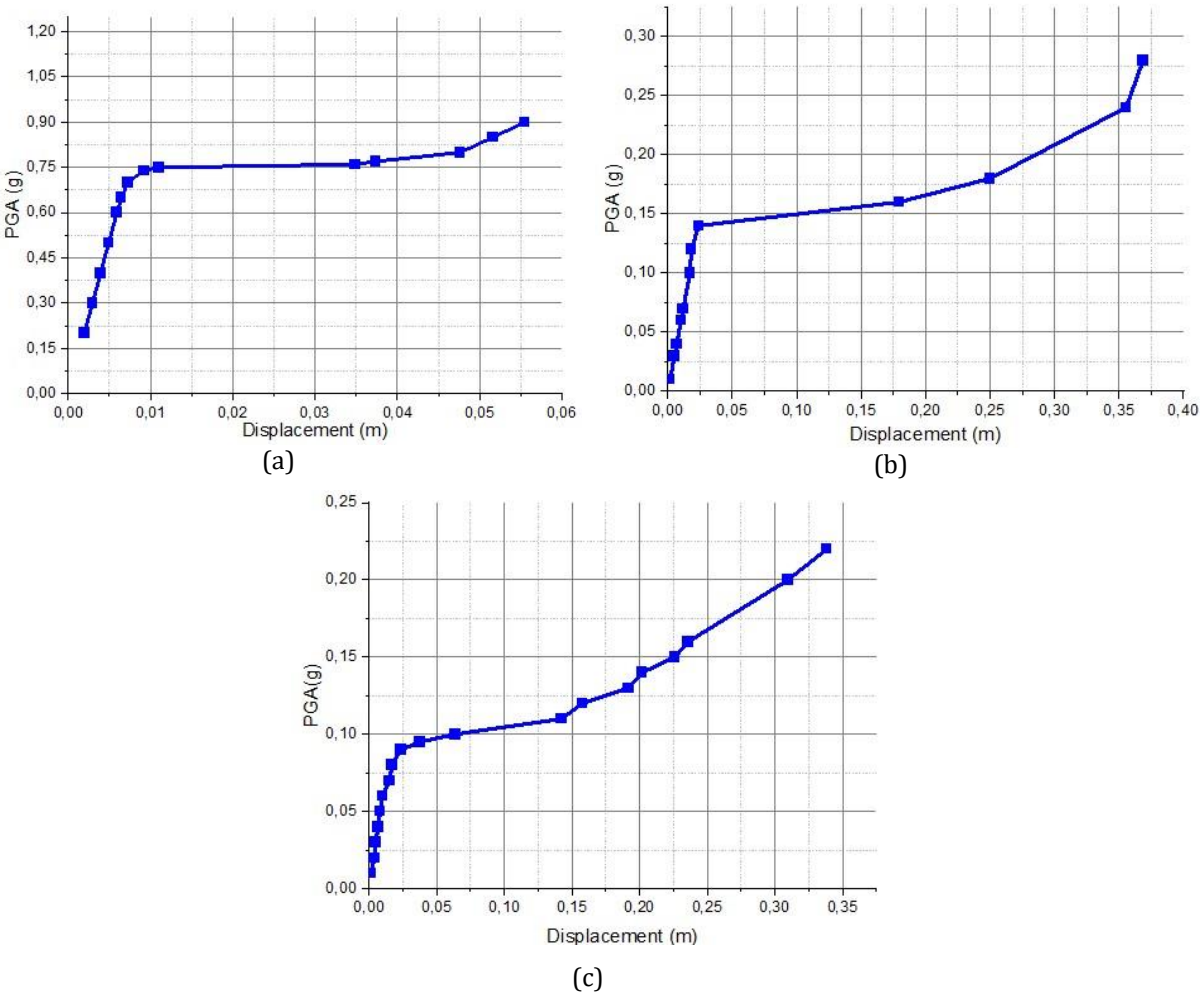

Fig. 7. Dynamic displacement response curves under selected earthquake ground motions: (a) San Fernando 1971, (b) Boumerdes 2003 (Dar El Beida), and (c) Parkfield 1966.

The peak response is illustrated in Fig. 7(a), which presents the maximum radial displacement as a function of increasing PGA, evaluated according to the Ari-Gur and Simonetta. For the model subjected to the San Fernando earthquake, the critical buckling PGA is identified at approximately

0.75 g. A sudden reduction in the slope of the displacement PGA curve marks the onset of shell buckling once the excitation exceeds this critical value.

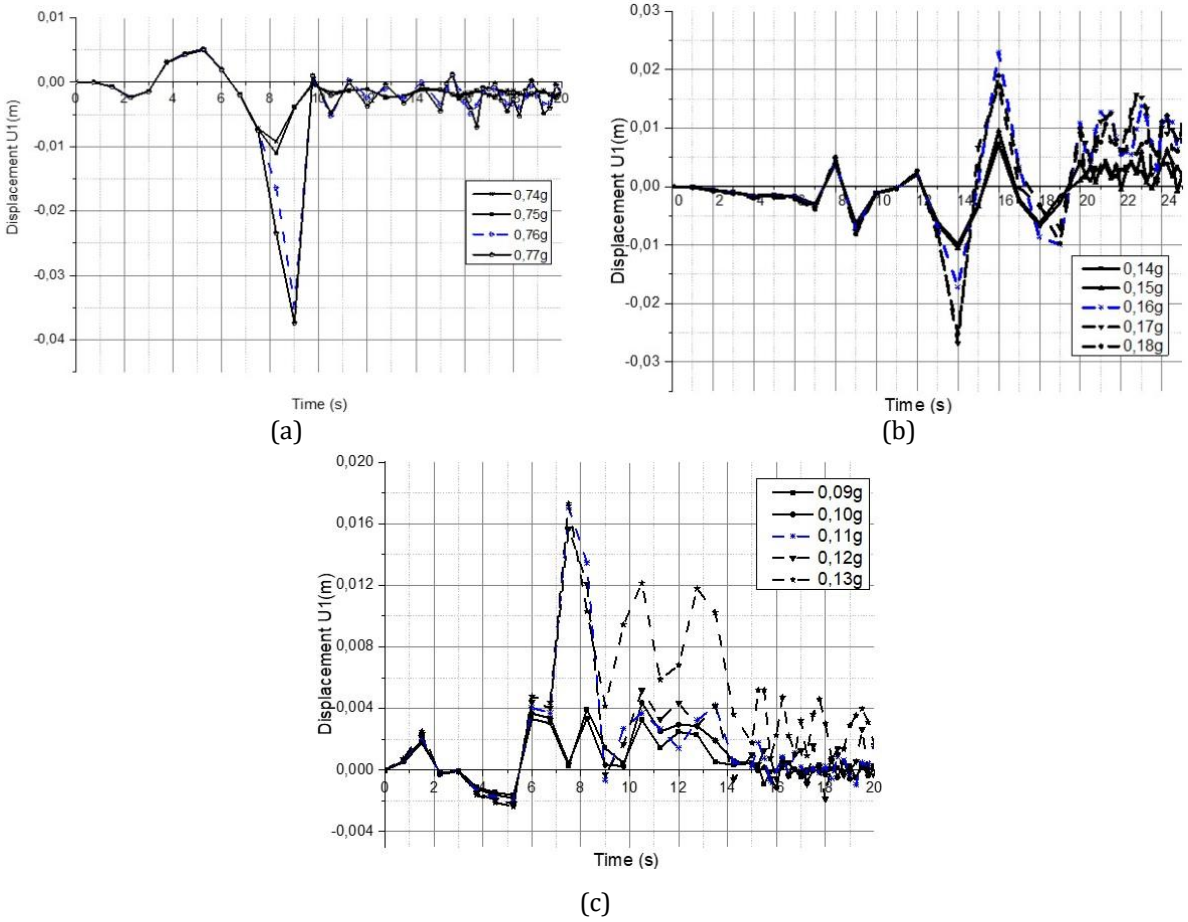

Fig. 8. Displacement Time Histories before and after PGAc under selected earthquake ground motions: (a) San Fernando 1971, (b) Boumerdes 2003 (Dar El Beida), and (c) Parkfield 1966.

Figures 8(a) present the displacement time histories obtained at the critical PGA level of 0.76 g, based on the Budiansky and Roth criterion, corroborating the observations from Fig. 7(a), where a pronounced jump in displacement is observed near the critical PGA, indicating the initiation of buckling. Further verification is provided in Fig. 9(a), which presents the phase-plane diagram (velocity–displacement) of the tank shell under the San Fernando earthquake. This diagram depicts the transition from stable to unstable structural behavior, confirming the identified onset of buckling.

For earthquakes characterized by dominant high-frequency content, the dynamic displacement response curves are presented in Figs. 7(b) and 7(c) for the Boumerdes (Dar El Beida, 2003) and Parkfield (1966) records, respectively. Critical buckling PGA values of approximately 0.15 g and 0.10 g are identified for the Boumerdes and Parkfield records, respectively. The same procedure for several values of the PGA for critical PGAc values and their corresponding deformed shape under earthquake of Boumerdes and Parkfield is shown in Figs. 7, 8 and 9 (b) and (c) respectively. The jump of peak response is observed at critical value 0.16g under earthquake of Boumerdes and at 0.11g under earthquake of Parkfield.

Figure 10 illustrates the evolution of the Von Mises stress at the critical location where buckling initiation occurs within the tank shell. These stress time histories are presented for increasing PGA levels across the San Fernando (1971), Boumerdes (Dar El Beida, 2003), and Parkfield (1966) earthquake records. For each ground motion, the stress time histories are shown for several PGA levels in the vicinity of the critical buckling acceleration. For the San Fernando earthquake (Fig. 10(a)), the stress response increases gradually with PGA up to approximately 0.75 g. At this level, a pronounced amplification of Von Mises stress is observed, characterized by a sharp peak followed

by stress redistribution. This behavior coincides with the critical PGA previously identified from displacement-based criteria and indicates the onset of shell instability.

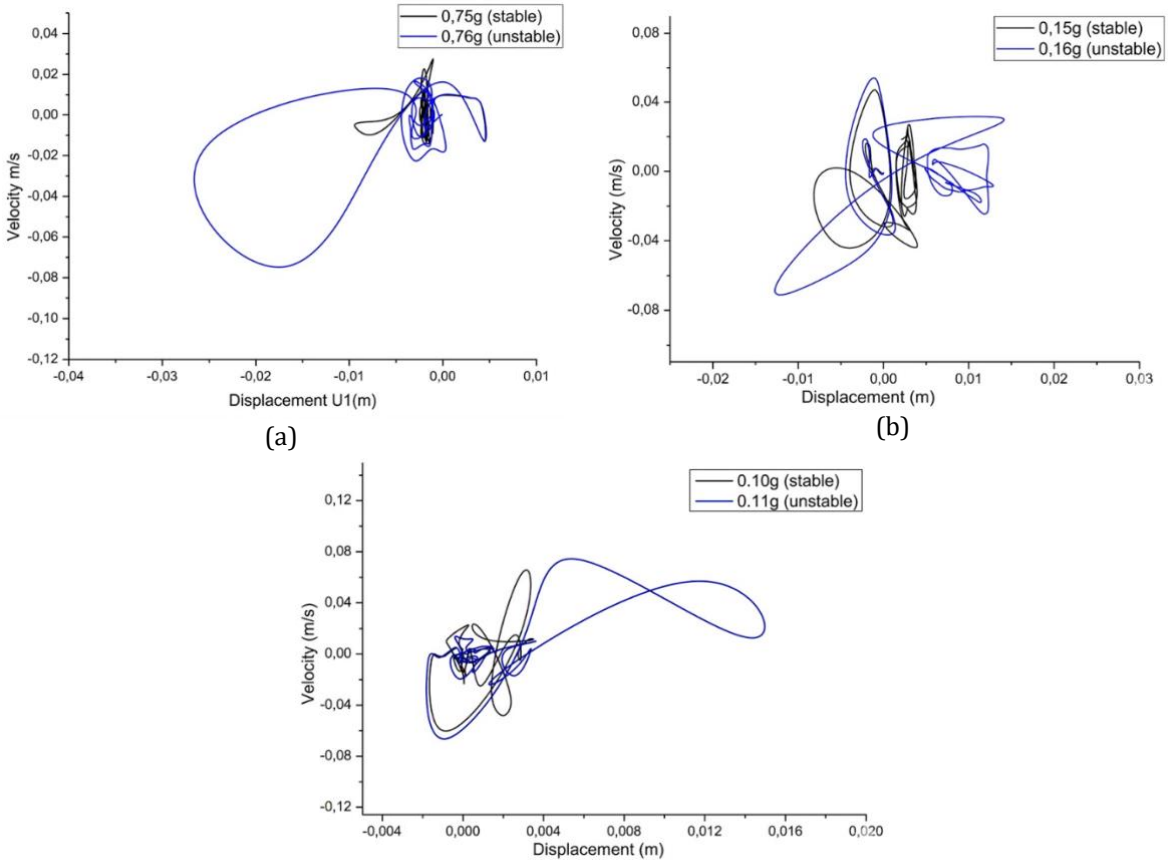

Fig. 9. Phase-plane representation before and after PGAc under: (a) San Fernando earthquake, (b) Boumerdes earthquake, (c) Parkfield earthquake

In contrast, the Boumerdes earthquake (Fig. 10(b)) exhibits a sharp increase in Von Mises stress at significantly lower PGA levels. A sudden rise in stress is observed near 0.16 g, corresponding to the critical buckling PGA identified from displacement jumps. This reflects the stronger interaction between the seismic frequency content of the Boumerdes record and the dominant vibration modes of the tank, leading to earlier stress concentration and instability despite the lower PGA level.

Similarly, the Parkfield earthquake (Fig. 10(c)) produces the earliest onset of critical stress conditions, with a marked stress amplification occurring at approximately 0.11 g. The sharp stress peak at this PGA indicates a highly dynamic response dominated by high-frequency components, which are particularly effective in triggering local shell vibrations. The lower critical PGA observed for Parkfield highlights the strong influence of frequency content on dynamic buckling susceptibility.

Overall, the Von Mises stress responses are consistent with the displacement Time Histories buckling criteria and confirm that dynamic buckling is governed not only by seismic intensity but also by the frequency characteristics of the input motion. Earthquakes with higher frequency content induce earlier stress localization and buckling at lower PGA levels, whereas records dominated by lower frequencies require higher PGA to reach instability.

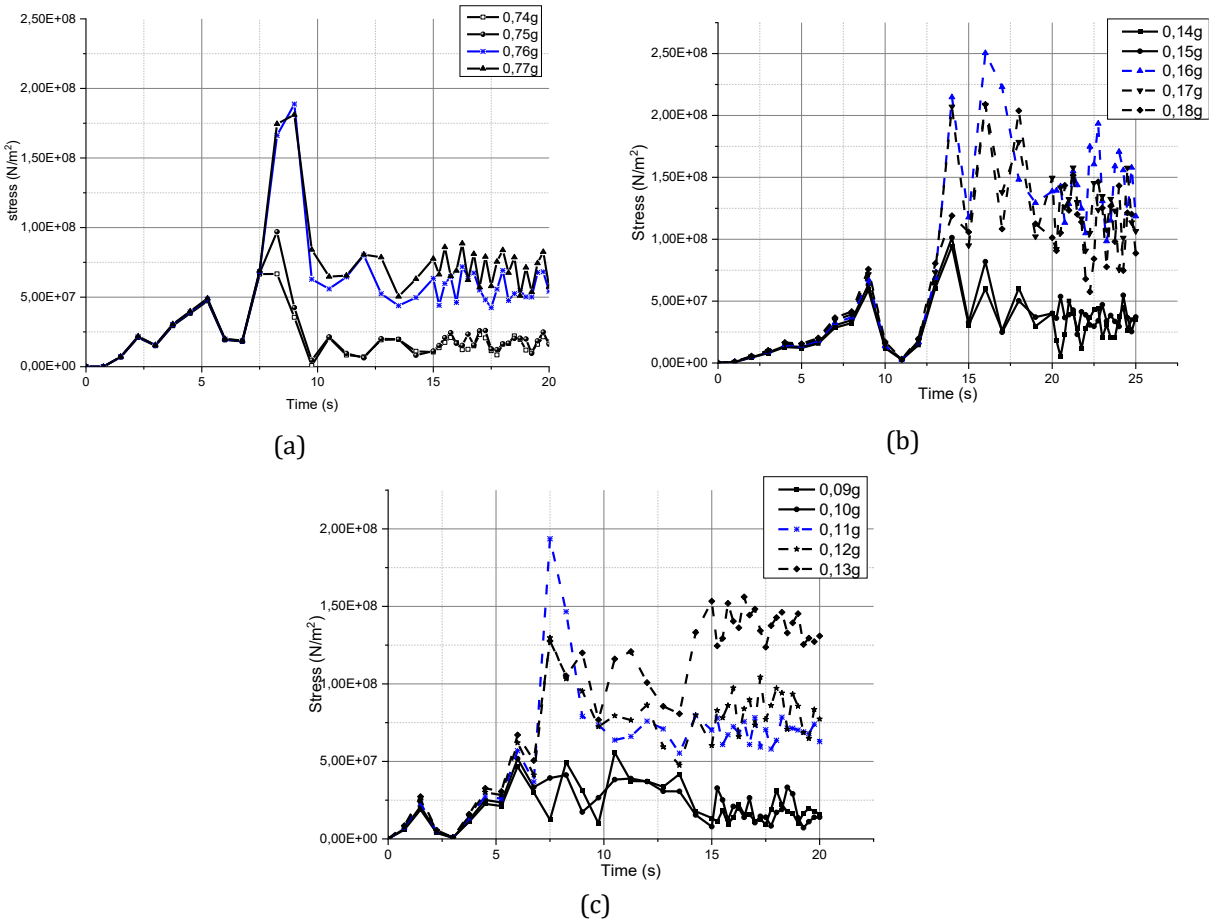

Fig. 10. Von Mises stress under of the selected earthquake ground motions: (a) San Fernando 1971, (b) Boumerdes 2003 (Dar El Beida), and (c) Parkfield 1966.

3.2 Buckling Patterns and Stresses

The nature of the dynamic buckling can be characterized by examining the deformed shape as well as the iso-stress contours at the critical level of excitation. Figure 14 shows the deformed tank exhibiting a partial depression at the top, which confirms a diamond-type buckling. The deformation patterns observed in diamond-type buckling are illustrated through the corresponding deformation shapes and contour plots (Figs. 11 and 12). The deformation patterns of the tank under dynamic loading clearly exhibit diamond-type buckling.

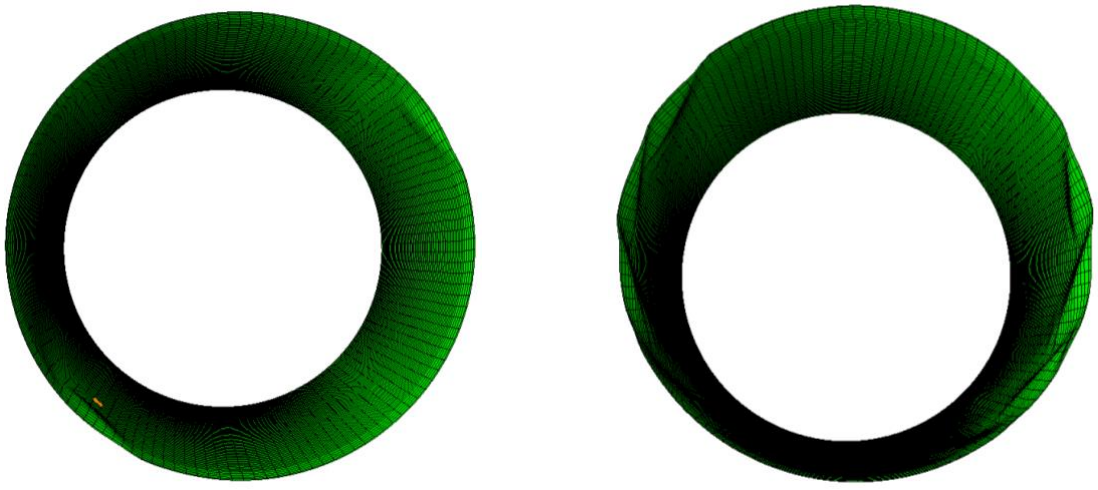

(a) (b)

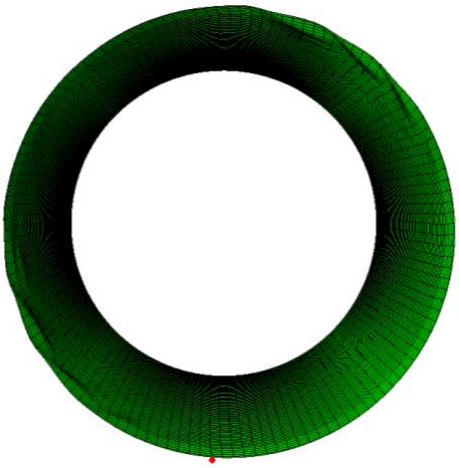

(c)

Fig. 11. Deformed shapes near the critical PGA for the (a) San Fernando, (b) Boumerdes, and (c) Parkfield earthquakes.

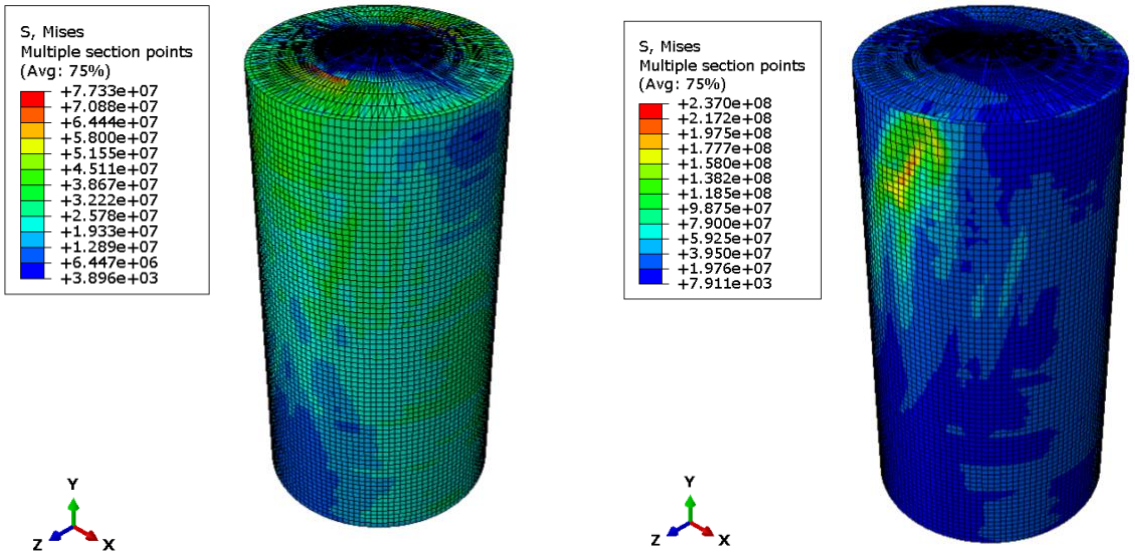

(a)

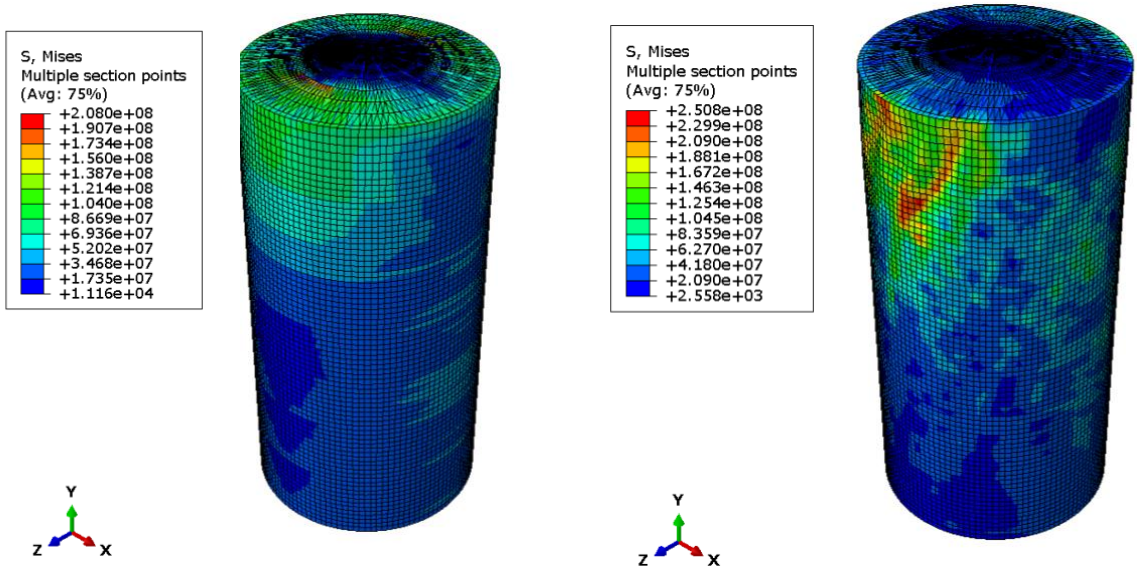

(b)

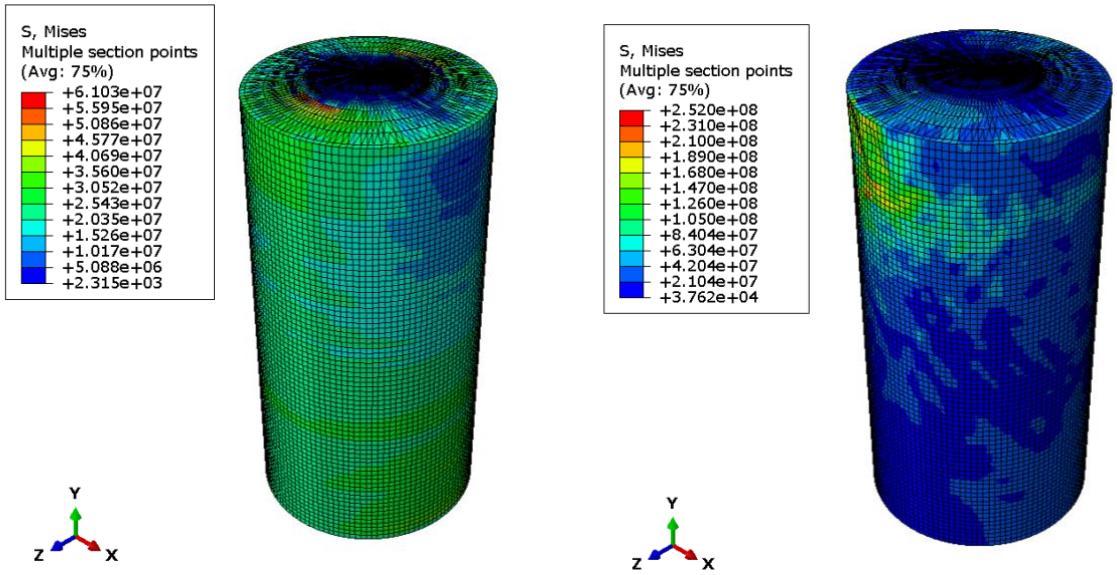

(c)

Fig. 12. Von Mises stress distribution before and after the critical PGA for the (a) San Fernando, (b) Boumerdes, and (c) Parkfield earthquakes, shown at the time of maximum peak response.

The shell shows characteristic inward and outward displacements forming circumferential lobes around the cylindrical surface, which are most pronounced at the instant of peak radial displacement. This instant represents the maximum response, when geometric instability is most apparent. The observed deformation remains consistent throughout the response, indicating that the buckling mode is governed by elastic shell behavior rather than post-yield phenomena such as elephant-foot buckling, which would require extensive plastic localization near the base.

The corresponding von Mises stress (see Fig .12) distribution highlights regions of stress concentration, typically at mid-height and near the top and bottom edges of the tank. At peak deformation, local stresses may approach or slightly exceed the steel's yield stress; however, yielding remains confined to small areas and does not modify the overall diamond-shaped deformation pattern. These stress contours provide valuable insight into the critical locations for potential material failure and serve as a key tool for validating numerical models against code predictions.

3.3 Effect of Seismic Frequency

The effect of seismic frequency on the dynamic response of thin-walled steel tanks is clearly observed when comparing the San Fernando (1971), Boumerdes (2003), and Parkfield (1966) earthquake records. For the San Fernando motion, characterized by intermediate-frequency content and a PGA/PGV ratio of 1.09, the phase-plane trajectory remains compact and nearly elliptical at low PGA, indicating stable oscillations of the tank. Critical dynamic buckling occurs around 0.75 g, where a sudden expansion of the trajectory is noted, indicating the transition to post-buckling behavior with nonlinear energy exchange between vibration modes. For the Boumerdes earthquake, which is characterized by high- and long-period frequency content and a moderate PGA/PGV ratio of 2.00, instability is triggered at a much lower PGA of approximately 0.16 g. Beyond this threshold, the phase-plane trajectory is observed to become distorted and scattered, indicating early loss of stiffness and asymmetric amplification of displacements and velocities, reflecting local dynamic effects. For the Parkfield record, which is dominated by high-frequency, short-period content with the highest PGA/PGV ratio of 2.30, the earliest onset of instability is observed at approximately 0.11 g. The phase-plane trajectory is observed to rapidly diverge from equilibrium, indicating amplified displacements and velocities associated with local shell vibrations and diamond-shaped buckling modes. These observations highlight that the frequency content of seismic excitations plays a critical role in determining the timing of dynamic buckling. Intermediate-frequency motions are observed to primarily activate local shell modes, leading to

higher critical PGA, whereas high-frequency motions are observed to primarily excite local shell instabilities, resulting in earlier buckling at lower PGA levels. Fourier amplitude spectra further confirm these distinctions, with San Fernando energy concentrated below 5 Hz, Boumerdes peaking around 3 Hz, and Parkfield distributing significant energy across 3–10 Hz. Overall, this analysis demonstrates that evaluating seismic response solely based on PGA may lead to an underestimation of the susceptibility of thin-walled tanks to high-frequency-induced local buckling, emphasizing the need to consider both amplitude and frequency characteristics in seismic design.

3.4 Comparison with Codes and Previous Studies

The discrepancies observed between design-code predictions and the numerical results obtained in this study can largely be attributed to differences in loading assumptions. Design codes typically determine elastic and plastic critical buckling stresses based on static analyses of cylindrical shells under uniform axial compression or a combination of axial compression and circumferential shear. These idealized conditions differ significantly from the dynamic seismic loading scenarios considered here, which helps explain the variations in critical buckling values. In addition, the results of the present study were compared with other numerical studies reported in the literature. Good agreement was observed, although the present study considers a slenderer tank (higher H/D ratio), which tends to buckle earlier than the tanks examined in previous studies. The critical buckling values adopted in Eurocode 8 [20], API 650 [21], and AWWA D100 [28]are summarized in Table 2.

Nonlinear dynamic simulations were conducted to determine the critical buckling PGA for the analyzed tanks and to compare these results with code-based estimates. Under the 1971 San Fernando earthquake, the simulations indicate a critical PGA of approximately 0.76 g. This value closely matches the results reported by Djermane [10] for a tank with H/D = 1. In the present study, the slightly earlier onset of buckling is due to the slenderer tank configuration (H/D = 2), which increases structural flexibility and promotes earlier instability. Design-code predictions for the same scenario are lower, with AWWA D100 estimating 0.27 g, while Eurocode 8 and API 650 provide 0.62 g and 0.55 g, respectively, reflecting the generally conservative nature of these standards.

Table 2. Comparison between numerical predictions and design guide values for critical stress and buckling

Standards	Numerical model	VIRELLA H/D=1	DJERMANE H/D=1	EC8	API	AWWA
Critical stress MPa	/	/	/	1.384E8	1.22E8	5.944E7
Critical buckling According to San Fernando	0.76g	/	1.00g	0.62g	0.55g	0.27g
Critical buckling According to Boumerdes	0.16g	/	/	0.09g	0.08g	0.04g
Critical buckling According to Parkfield	0.11g	0.20g	1.07g	0.08g	0.07g	0.04g

For the 2003 Boumerdes earthquake, the numerical analysis reveals critical PGA reductions of approximately −50% and −75% relative to API 650 and AWWA D100, respectively, further highlighting the conservative nature of code-based design approaches. In the case of the 2004 Parkfield earthquake, dynamic buckling occurs at 0.11 g. This value is slightly lower than that reported by Virella (Virella et al., 2006) for a tank with H/D = 1, owing to the increased flexibility of the slender tank configuration. Comparisons with code predictions indicate that Eurocode 8 yields 0.08 g, corresponding to a deviation of −27%, API 650 provides a similar estimate, and AWWA D100 gives a substantially lower value of 0.04 g. These results collectively emphasize that detailed nonlinear dynamic simulations provide a more realistic prediction of buckling behavior under seismic loading. In contrast, design-code-based approaches tend to be more conservative,

particularly for slender tanks, underscoring the importance of accounting for dynamic effects and geometry when evaluating structural stability under earthquake excitations.

4. Conclusion

The present numerical investigation has demonstrated that tall thin-walled cylindrical steel tanks exhibit a high sensitivity to both the intensity and frequency content of seismic excitations. A clear correlation was observed between critical buckling loads and the characteristics of the applied ground motions. In particular, the San Fernando (1971) earthquake, characterized by intermediate-frequency content and a PGA/PGV ratio of 1.09, was found to induce buckling at a PGA of approximately 0.76 g, which is in close agreement with predictions provided by Eurocode 8, exhibiting only a 18% deviation. In contrast, the Boumerdes (2003) and Parkfield (1966) ground motions, which contain substantial high-frequency components and exhibit higher PGA/PGV ratios, were associated with significantly lower critical PGA values of 0.16 g and 0.11 g, respectively. These findings indicate that the frequency content of seismic records exerts a pronounced influence on the dynamic stability and local buckling behavior of tall thin-walled tanks, often resulting in the onset of instability at lower PGA levels than predicted by static or quasi-static code-based formulations.

The observed elastic diamond-shaped local buckling near the top region of the tank walls was found to be consistent with previously reported experimental and numerical studies, confirming that instability tends to initiate in regions where bending moments are high and axial stiffness is reduced. Fourier analysis of the earthquake records further demonstrates that local shell instabilities and diamond-shaped buckling are triggered under both frequency ranges. However, the buckling of the tank is predominantly delayed under intermediate-frequency motions. In contrast, earlier triggering of the same buckling patterns is observed under high-frequency excitations, with critical thresholds being reached at significantly lower PGA values. It is therefore demonstrated that PGA alone is insufficient for the accurate assessment of seismic-induced buckling risk, and that the spectral content and the duration of seismic motions must also be considered.

Finally, the present work provides a structured framework for future research aimed at enhancing the seismic performance of cylindrical steel tanks. It is suggested that subsequent investigations involve a larger set of seismic records, including more than twenty motions, to more comprehensively evaluate the influence of frequency characteristics on dynamic buckling. Additionally, mitigation strategies, such as the incorporation of stiffening rings, could be explored to reduce the susceptibility of tanks to diamond-shaped local buckling. By explicitly defining the tank configuration, identifying its vulnerable regions, and systematically examining the effects of seismic frequency content, this study establishes a solid foundation for performance-based design approaches that go beyond simplified static criteria, ultimately contributing to the improved safety and reliability of storage tanks under earthquake loading.

Nomenclature

D	Tank diameter(m)	$\ddot{x}_g$	Ground acceleration m/s^2
R	Tank radius (m)	ρ	Density equivalent
H	Tank height (m)	PGA	Peak ground acceleration (g)
T	Tank shell thicknesses	PGA_c	Critical peak ground acceleration (g)
ν	Poisson ratio	t	Time (s)

References

[1] Jain SK, LETTIS WR, MURTY CVR, et al. Bhuj, India earthquake of January 26, 2001, reconnaissance report. Earthquake Spectra 2002;18. https://doi.org/10.1193/1.2803902

[2] Suzuki K. Report on damage to industrial facilities in the 1999 Kocaeli earthquake, Turkey. Journal of Earthquake Engineering 2002;6:275-96. https://doi.org/10.1080/13632460209350417

[3] Cooper TW, Wachholz TP. Optimizing post-earthquake lifeline system reliability. Proceedings of the 5th US conference on lifeline earthquake engineering. ASCE, vol. 16, 1999, p. 878-86.

[4] Zhang YL, Reese JM, Gorman DG. Finite element analysis of the vibratory characteristics of cylindrical shells conveying fluid. Comput Methods Appl Mech Eng 2002;191:5207-31. https://doi.org/10.1016/S0045-7825(02)00456-5
[5] Shen H-S. Postbuckling of shear deformable cross-ply laminated cylindrical shells under combined external pressure and axial compression. Int J Mech Sci 2001;43:2493-523. https://doi.org/10.1016/S0020-7403(01)00058-3
[6] Virella JC, Godoy LA, Suárez LE. Fundamental modes of tank-liquid systems under horizontal motions. Eng Struct 2006;28:1450-61. https://doi.org/10.1016/j.engstruct.2005.12.016
[7] Virella JC, Godoy LA, Suárez LE. Dynamic buckling of anchored steel tanks subjected to horizontal earthquake excitation. J Constr Steel Res 2006;62:521-31. https://doi.org/10.1016/j.jcsr.2005.10.001
[8] Virella JC, Suárez LE, Godoy LA. A static nonlinear procedure for the evaluation of the elastic buckling of anchored steel tanks due to earthquakes. Journal of Earthquake Engineering 2008;12:999-1022. https://doi.org/10.1080/13632460701672714
[9] Buratti N, Tavano M. Dynamic buckling and seismic fragility of anchored steel tanks by the added mass method. Earthq Eng Struct Dyn 2014;43:1-21. https://doi.org/10.1002/eqe.2326
[10] Djermane M, Zaoui D, Labbaci B, et al. Dynamic buckling of steel tanks under seismic excitation: Numerical evaluation of code provisions. Eng Struct 2014;70:181-96. https://doi.org/10.1016/j.engstruct.2014.03.037
[11] Sobhan MS, Rofooei FR, Attari NKA. Buckling behavior of the anchored steel tanks under horizontal and vertical ground motions using static pushover and incremental dynamic analyses. Thin-Walled Structures 2017;112:173-83. https://doi.org/10.1016/j.tws.2016.12.022
[12] Sobhan MS, Hosseini P. A Study of the Buckling Behavior of Aboveground Cylindrical Steel Tank under Seismic Loading. Civil Infrastructure Researches 2022;8:21-34.
[13] Çelik Aİ, Köse MM. Dynamic buckling analysis of cylindrical steel water storage tanks subjected to Kobe earthquake loading. Steel Construction 2020;13:128-38. https://doi.org/10.1002/stco.201900003
[14] Yasunaga J, Uematsu Y. Dynamic buckling of cylindrical storage tanks under fluctuating wind loading. Thin-Walled Structures 2020;150:106677. https://doi.org/10.1016/j.tws.2020.106677
[15] Djelloul NDH, Djermane M, Sharari N. Non-linear numerical study of the dynamic response of elevated steel conical tank under seismic excitation. Revista Romana de Inginerie Civila 2022;13:272-88. https://doi.org/10.37789/rjce.2022.13.3.5
[16] Moreno M, Colombo J, Wilches J, et al. Buckling of steel tanks under earthquake loading: Code provisions vs FEM comparison. J Constr Steel Res 2023;209:108042. https://doi.org/10.1016/j.jcsr.2023.108042
[17] Ullah S, Mamaghani IHP. Numerical Investigation on Buckling Response of Cylindrical Steel Storage Tanks Under Seismic Excitation. Ce/Papers 2023;6:343-7. https://doi.org/10.1002/cepa.1999
[18] Abd-Elhamed A, Mahmoud S. Seismic assessment of cylindrical storage tanks to records with different frequency contents considering fluid-structure-soil/foundation interaction. Journal of Low Frequency Noise, Vibration and Active Control 2025;44:54-80. https://doi.org/10.1177/14613484241275593
[19] Nadjuri A, Setiawan R, Rildova R, et al. Earthquake-Induced Sloshing Response of Above-Ground Storage Tank with Various Roof Types and Slenderness. Available at SSRN 5807722 2025. https://doi.org/10.2139/ssrn.5807722
[20] Standard B. Eurocode 8: Design of structures for earthquake resistance. Part 2005;1:1991-8.
[21] Standard API. Welded steel tanks for oil storage 1988.
[22] EN 1993-1-6:2007/A1:2017 - Eurocode 3 - Design of steel structures - Part 1-6: Strength and Stability of Shell Structures n.d.
[23] Sadowski AJ, Rotter JM. Solid or shell finite elements to model thick cylindrical tubes and shells under global bending. Int J Mech Sci 2013;74:143-53. https://doi.org/10.1016/j.ijmecsci.2013.05.008
[24] Abaqus G. Abaqus 6.11. Dassault Systemes Simulia Corporation, Providence, RI, USA 2011;3:73.
[25] Kumar H, Saha SK. Effects of uncertain soil parameters on seismic responses of fixed base and base-isolated liquid storage tanks. Journal of Earthquake Engineering 2024;28:176-201. https://doi.org/10.1080/13632469.2023.2195017
[26] Zulfiqar Y, Hyder MJ, Jehanzeb A, et al. Numerical investigation of an optimum ring baffle design to optimize the structural strength of a tank subjected to resonant seismic sloshing. Structural Engineering International 2023;33:350-60. https://doi.org/10.1080/10168664.2022.2029690
[27] Budiansky B. Axisymmetric dynamic buckling of clamped shallow spherical shells. NASA TN 1962;1510:597-606.
[28] Association AWW. Welded steel tanks for water storage. Colorado, USA 1997.